Supporting Information

Light-modulated van der Waals force microscopy

Yu-Xiao Han, Benfeng Bai[*], Jian-Yu Zhang, Jia-Tai Huang, Peng-Yi Feng, Hong-Bo Sun[*]

State Key Laboratory of Precision Measurement Technology and Instruments, Department of Precision Instrument,

Tsinghua University, Beijing 100084, China.

Corresponding author: baibenfeng@tsinghua.edu.cn; hbsun@tsinghua.edu.cn.

SI-1. Difference of LvFM with other microscopic methods

Different from AFM and other scanning probe microscopy methods such as scanning near-field optical microscopy (SNOM)[1,2], the light-modulated van der Waals force microscopy (LvFM) can be regarded as an optical version of AFM that uses a tapping-mode AFM probe working in the tip-sample van der Waals (vdW) force interaction zone to probe the subtle tip-sample force change caused by local molecular thermal fluctuation of materials under light illumination. Since different materials have different intermolecular binding forces and hence different optothermal responses, the detected LvF contrast in different regions of a sample can reflect the compositional information of it. Based on this principle, the composing materials of a sample can be discriminated provided that the detected LvF contrast is distinguishable.

To characterize heterostructures of nanomaterials, some high-resolution microscopic methods such as scanning electron microscopy (SEM) and scanning tunneling microscopy (STM) have been used to characterize nanoscale regions that may lead to an increase or decrease of the electric conductivity of materials[3,4]. However, despite the high spatial resolution of these methods for topography mapping, they have to be implemented in vacuum and cannot provide information about the associated electronic, spin, and optical responses of materials.

AFM, though powerful in profiling surface features of samples with very high resolution, cannot probe the compositional information of materials. In the past decades, AFM has been combined with other techniques to study the dynamic, thermodynamic, optical, electric, magnetic, and chemical properties of materials[5]. For example, in order to characterize the chemical composition of materials, a technique called AFM-based infrared spectroscopy (AFM-IR)[6] has been developed, which integrates the chemical analysis capability of infrared spectroscopy and the high spatial resolution of AFM. AFM-IR uses an AFM tip to probe the local thermal expansion of material caused by molecular vibrational absorption of infrared light[7]. Since molecular vibrational absorption usually occurs within the conduction band or valence band, it is associated with an intraband transition. Under infrared light excitation, the thermal expansion of sample surface may trigger the mechanical vibration of the probe usually working in contact mode on a sample surface, from which the probe vibration response is analyzed to obtain the composition of the sample. As per the AFM-IR principle, the optothermal expansion of materials, such as polymers[6], biological tissues[7], and organics[8], should be large enough to be detectable. For this reason, the excitation light wavelength should be chosen to coincide with the molecular absorption energy transition levels (usually in infrared band) so as to produce a series of narrow fingerprint peaks with sufficiently large imaging contrast and signal-to-noise ratio (SNR). Nevertheless, due to the limitation of excitation laser power and the damage threshold of some materials, many samples cannot produce sufficiently large thermal expansion for AFM-IR. These restrict the application scenarios of AFM-

IR. Unlike AFM-IR, LvFM can respond to extremely small fluctuation of molecular thermal motions based on its vdW force sensing mechanism. Therefore, the light absorption in materials through non-radiative interband transition can be utilized, although it is usually much weaker than the molecular vibrational absorption in AFM-IR. Different from intraband absorption, the interband absorption is non-resonant, which produces a wide absorption band covering the visible and infrared regime. This feature greatly facilitates the choice of excitation light source in LvFM.

In addition to the above methods, there are some other near-field optical techniques such as tip-enhanced photoluminescence (TEPL)[9] and tip-enhanced Raman scattering (TERS)[10] that can be used to characterize the chemical composition of materials. However, these methods have to rely on both the emission (photoluminescence or Raman) properties of materials and spectroscopic scanning. In this regard, LvFM does not need to collect any optical signal from the sample (except for the mechanical vibration of the cantilever monitored by the optical lever) and does not need to use spectrometer as well. It is thus a rather simple and versatile method for discriminating a wide range of materials including metals, dielectrics, semiconductors, and various nanomaterials such as 2D materials, as shown below in the various characterization experiments.

In recent years, a near-field technique called photo-induced force microscopy (PiFM) has been proposed, which combines the advantages of AFM and near-field spectroscopy to perform near-field characterization with high spatial and spectral resolutions[11]. The principle of PiFM is to detect the mechanical force generated between a photo-induced dipole at the sample surface and a mirror dipole in the AFM tip[12]. The mechanical vibration of the cantilever is driven by a dither piezo and modulated by a laser beam irradiating the tip-sample gap. The AFM probe works in non-contact mode, so that the net force between tip and sample is attractive. Different from the vdW force sensing mechanism of LvFM, the dipole-dipole interaction force in PiFM is dominant only in materials with large polarizability and is also sensitive to the wavelength of illumination light. PiFM can use direct demodulation or sideband demodulation, where the setpoint is usually set at ~85%. In comparison, LvFM makes use of LvF, which is a universal force existing between any sample and the probe tip. Therefore, in principle, LvFM has no special requirement on sample material and excitation light, provided that the thermal motion of molecules of the sample can be enhanced by light excitation. In this sense, LvFM can be applied to a wider range of materials, including metals, dielectrics, semiconductors, and ultra-thin nanomaterials such as 2D materials, as will be shown in the following sections. Moreover, since LvFM works across the vdW force interaction zone, it requires a closer tip-sample distance than PiFM, so that the tapping mode is adopted with the setpoint usually set at ~60% and a sideband demodulation technique based on dual-modal cantilever is used to extract the LvF signal.

With the above comparison and discussions, it is seen that LvFM is a brand-new non-radiative, non-destructive, and non-spectroscopic near-field method for super-resolution imaging of heterogenous composition of materials through near-field LvF detection.

SI-2. The tip-sample interaction forces in tapping mode

In AFM, many forces play roles in the tip-sample interaction process. As shown in the left panel of Fig. S1., the dominating interaction forces can be attributed to different categories according to the tip-sample distance, among which the chemical interaction force, the vdW force, the electrostatic force are three commonly existing forces playing main roles in AFM[5]. The chemical interaction force is a short-range repulsive force caused by Pauli repulsion. The vdW force and electrostatic

force take effect in longer range and stay attractive as the tip approaches the sample surface, among which the interaction range of electrostatic force is wider and the vdW force commonly existing in various materials.
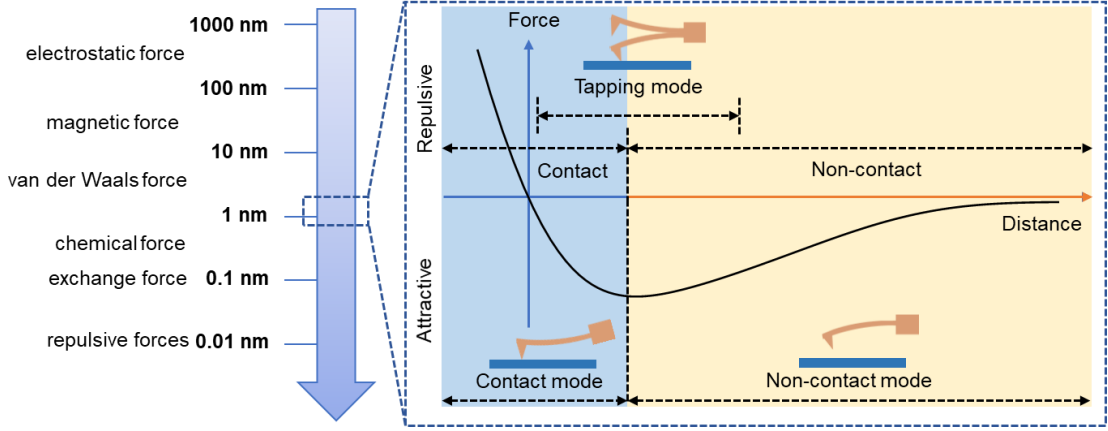

Fig. S1. Various distance-dependent tip-sample interaction forces. Left panel: various long- and short-range interaction forces between the tip and sample. Right panel: the distance-dependent interaction force curve of an AFM probe where three working modes (contact, non-contact, and tapping) are indicated.

The right panel of Fig. S1 depicts the relationship of the interaction force versus tip-sample distance at the region where the vdW force and partly chemical force are dominant. At different distances, the total force may be attractive or repulsive, depending on whether the attractive vdW force or the repulsive contact force are dominant. Correspondingly, the force curve can be divided into two regions, the non-contact region the and contact region, according to whether the gradient of the force curve is positive or negative, respectively. When the AFM probe works in tapping mode, it reciprocates in the non-contact and contact regions and the attractive and repulsive forces act alternately on the probe tip.

SI-3. Numerical calculation of the tip-sample interaction force

We established a model to describe and analyze the interaction force between an AFM tip and a flat sample surface when they are very close to each other. Details of such calculations have been reported in many previous literatures[13,14]. The force between two closely spaced molecules can be expressed as Eq. (1) in the main text. Owing to the additivity of vdW force, the total tip-sample force can be calculated from the contributions of all molecules in the tip and sample, shown as the integration in Eq. (2) in the main text. A schematic diagram of the calculation is shown in Fig. S2, where the sample is simplified as a flat plate of thickness d, and the tip apex is regarded as a hemisphere with radius R. The position coordinate of an atom in the tip (such as point A in Fig. S2)can be written as A($r_t\cos\alpha\cos\beta$, $r_t\cos\alpha\sin\beta$, $r_t\sin\alpha$), where r_t is the radial distance of point A, and α and β are the polar angle and azimuthal angle of it in the spherical coordinate system, respectively. The position coordinate of an atom in the sample (such as point B in Fig. S2) can be written as B($\rho\cos\zeta$, $\rho\sin\zeta$, z), where ρ is the distance of projection of point B and ζ is the azimuthal angle of it in the cylindrical coordinate system. So, the distance between the two atoms can be expressed as

$$r = \sqrt{(\cos\alpha\cos\beta r_t - \cos\zeta\rho)^2 + (\cos\alpha\sin\beta r_t - \sin\zeta\rho)^2 + (sin\alpha r_t - z)^2} \ . \qquad (S1)$$

Then the Lennard-Jones force f_{LJ} between atom A and atom B can be calculated by Eq. (1) in

the main text. The total tip-sample force can then be calculated by Eq. (2), which yields

$$F = \int_h^{h+d} \int_0^{2\pi} \int_0^{+\infty} (\int_0^{\pi/2} \int_0^{2\pi} \int_0^R n_2 f_{LJ}(r(\alpha,\beta,r_t,\zeta,\rho,z))dr_t d\alpha d\beta) d\rho d\zeta dz , \qquad (S2)$$

where n_2 is the molecule density of the sample, and h is the distance between the tip apex and sample surface.

According to Eqs. (1), (2), (S1), and (S2), the tip-sample interaction force can be calculated for h ranging from 0.3 nm to 15 nm, as shown by the blue curve in Fig. 1(b). The calculation was performed with $\varepsilon = 1\times10^{-19}$ J and $r_0 = 0.3$ nm, which are estimated values applicable to most materials. The probe tip radius is taken as $R=10$ nm. The step size (mesh precision) used in the calculation is 0.5 nm.
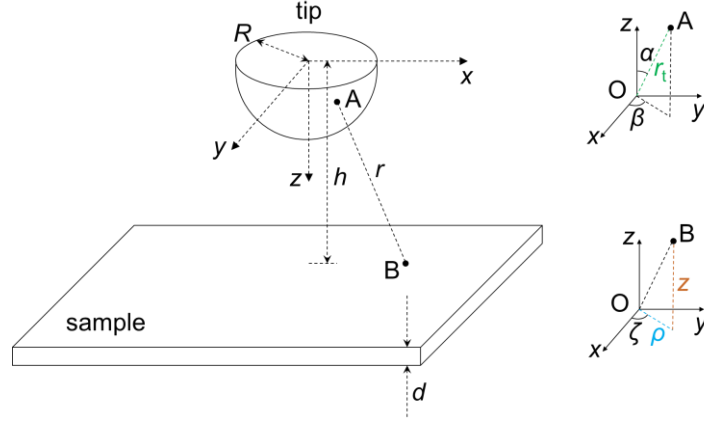

Fig. S2. Theoretical model of calculating the vdW force between a tip and a flat sample surface.

SI-4. Calculation of the temperature rise in the sample

With light illumination, the thermal motions of molecules on a sample surface are intensified, which lead to local temperature rise in the illuminated region of the sample. The temperature rise can be modeled by the heat diffusion equation[15] with a heat source $Q(t)$:

$$\rho C \frac{dT}{dt} = \frac{Q(t)}{V(t)} - \kappa_{eff} \nabla^2 T(\rho,z,t) , \qquad (S3)$$

where ρ, C, $T(\rho,z,t)$, and κ_{eff} are the density, heat capacity, Kelvin temperature, and effective thermal conductivity[16] of the sample material, respectively, and $V(t) = V_p(t) + V_a(t) + V_d(t)$ is the volume of the sample affected by the optothermal effect, as shown in SI-7.

In LvFM, the excitation laser is modulated at frequency f_m, which can be described by a function of rectangular pulses of duration τ_{pulse}. Then the heating source can be expressed as

$$Q(t) = P_{abs} M(\tau_{pulse}) , \qquad (S4)$$

where P_{abs} is the absorbed light power and $M(\tau_{pulse})$ is a rectangular box function of length τ_{pulse}[15]. For most materials, the absorption of light is determined by the imaginary part of the complex permittivity. Then the absorbed light power can be expressed as

$$P_{abs} = \int \frac{1}{2} \omega |E|^2 \operatorname{Im}(\varepsilon)dV , \qquad (S5)$$

where ω, $|E|$, and $\operatorname{Im}(\varepsilon)$ are the light frequency, the electric field amplitude on the sample surface, and the imaginary part of the material complex permittivity, respectively. The integral covers the entire volume illuminated by the light.

Rigorous modeling of this optothermal process requires complete multi-dimensional solution of Eq. (S3) to get the temperature distribution in the sample. By ignoring the heat accumulation and heat dissipation in substrate and in air around the sample, the model can be simplified so that the temperature under the probe apex can be estimated as[16]

$$T(0,z,t) = T_0 + \Delta T_{\max} \frac{1 - e^{-t/\tau_{\mathrm{rel}}}}{1 - e^{-\tau_{\mathrm{pulse}}/\tau_{\mathrm{rel}}}} \cos(\zeta z / d) \quad (t < \tau_{\mathrm{pulse}}), \qquad (S6)$$

$$T(0,z,t) = T_0 + \Delta T_{\max} e^{-(t-\tau_{\mathrm{pulse}})/\tau_{\mathrm{rel}}} \cos(\zeta z / d) \quad (t > \tau_{\mathrm{pulse}}), \qquad (S7)$$

where T_0, $\Delta T_{\max}$, τ_{rel}, ζ, and d are the ambient temperature, the maximum temperature variation, the thermal relaxation (cooling) time, the thermal mode shape factor, and the thickness of the sample, respectively. $\Delta T_{\max}$ can be estimated as $\Delta T_{\max} \approx \tau_{\mathrm{rel}} P_{\mathrm{abs}}/\rho CV$ for $\tau_{\mathrm{rel}} < \tau_{\mathrm{pulse}}$ and $\Delta T_{\max} \approx \tau_{\mathrm{pulse}} P_{\mathrm{abs}}/\rho CV$ for $\tau_{\mathrm{rel}} > \tau_{\mathrm{pulse}}$. τ_{rel} represents the time of heat equilibrium between the sample and the environment in the thermal diffusion process. In the absence of inter-facial thermal resistance, τ_{rel} is given by the following equation[16]

$$\tau_{\mathrm{rel}} \approx \frac{4}{\pi^2} \frac{C\rho d^2}{\kappa_{\mathrm{eff}}}. \qquad (S8)$$

The temperature rise is then a manifestation of the intensified motions of sample molecules under light illumination.

SI-5. Theoretical analysis of the light-modulated van der Waals force (LvF)

The static vdW force can be calculated by Eqs. (1) and (2). When a light beam illuminates the sample, the excited LvF between the probe tip and the sample can be calculated as follows.

Generally, the probe's equilibrium working position h is much higher than the repulsive force zone so that the total force F is an attractive force. Considering this fact, to facilitate analysis, we can neglect the second repulsive force term in Eq. (1) and substitute it into Eq. (2), which yields

$$f = n_2 \int_0^{+\infty} 2\pi\rho d\rho \int_h^{+\infty} \frac{z}{\sqrt{\rho^2 + z^2}} \frac{6\varepsilon r_0^6}{\left(\sqrt{\rho^2 + z^2}\right)^7} dz ,$$

$$= \frac{\pi n_2 \varepsilon r_0^6}{12h^4} \qquad (S9)$$

where ρ and z are coordinates defined in Fig. 1a.

When light illuminates the sample surface, the thermal motions of the sample molecules are intensified. To describe the irregular thermal motion of a molecule located at (ρ, z) and at moment t, we define a random displacement vector $\mathbf{u}(\rho, z, t)$, as shown in the inset of Fig. 1(a), whose direction is always along $\mathbf{r}$, i.e., toward the tip apex. Taking this random molecular displacement into consideration, we can rewrite Eq. (S9) as

$$f' = n_2 \int_0^{+\infty} 2\pi\rho d\rho \int_h^{+\infty} \frac{z}{\sqrt{\rho^2 + z^2} + u(\rho,z,t)} \frac{6\varepsilon r_0^6}{\left(\sqrt{\rho^2 + z^2} + u(\rho,z,t)\right)^7} dz$$

$$\triangleq \frac{\pi n_2 \varepsilon r_0^6}{12(h - \triangle h)^4} \qquad (S10)$$

$$\approx \frac{\pi n_2 \varepsilon r_0^6}{12h^4} + \frac{\pi n_2 \varepsilon r_0^6}{3h^5} \triangle h$$

.

Clearly, according to Eq. (S10), when a sample molecule moves closer to the probe tip under light excitation, the vdW force f' will increase, due to the decrease of the tip-molecule distance to $h-\Delta h$. On the contrary, when the molecule moves farther away from the tip in the other half of its oscillation cycle, f' will decrease due to the increase of $h+\Delta h$. However, since f' has a high-order nonlinear dependence ($\propto h^{-4}$) on h, the integration of f' in one cycle of the molecule oscillation leads to the increase of the overall tip-molecule vdW force, which can be numerically validated, as shown in Fig. 1(c). Having obtained f'', we can substitute Eq. (S10) into Eq. (2) and calculate the total tip-sample vdW force F' by numerical integration. Since the probe tip in LvFM works in tapping mode, the tip-sample forces vary periodically in accordance with the cantilever oscillation. So, we can calculate F or F' in a period and take their average values as the total forces.

Moreover, in the condition of thin sample thickness ($d < \lambda$) and low power laser irradiation, Δh is nearly proportional to the temperature rise ΔT under the tip apex, which is described as

$$\Delta h = \mu d \Delta T = \mu d [T(0, z, t) - T_0], \tag{S11}$$

where μ is the thermal expansion coefficient of material. This indicates that with the increase of excitation light power, the local temperature rise of material will lead to stronger thermal motions of molecules to increase Δh, and consequently the LvF is enhanced.

As for the mechanism of LvFM discriminating different materials, it arises from the different intermolecular binding forces of materials, as illustrated in Fig. S3. Let us consider two materials with different binding forces (sample 1 > sample 2). When light illuminates the samples, the molecular thermal motions are enhanced so that $A_2 > A_1$. Consequently, the tip-sample vdW forces $f_2 > f_1$. For two samples with the same light excitation, $f_3 > f_2$ because of $A_3 > A_2$. This shows why the LvF is intrinsic to material and can be used to identify different materials, which are also validated by experimental results in Fig. 3 and Fig. 4.
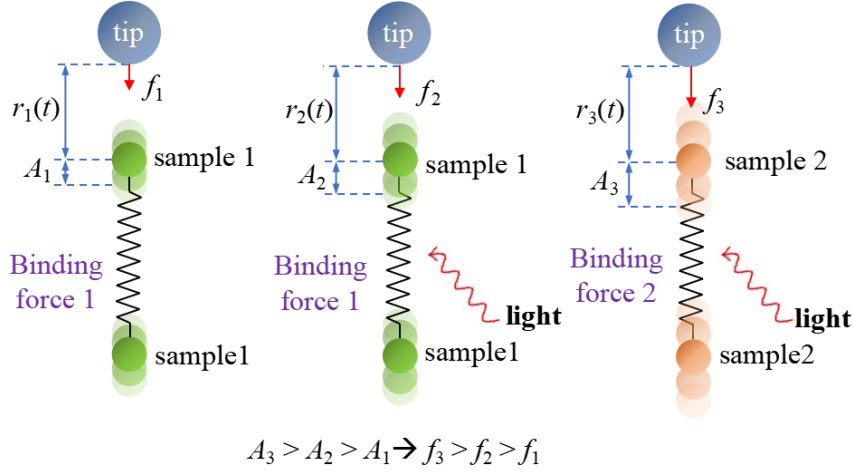

Fig. S3. Illustration of the intermolecular binding forces of two different materials with or without light excitation.

SI-6. Mechanical resonances of the dual-modal cantilever

A dual-modal AFM cantilever is used in the LvFM setup. The mechanical resonance frequencies of the first- and second-order eigenmodes of the cantilever are denoted as f_1 and f_2, respectively. In our operation, the tapping frequency of the probe tip is set as $f_1 = 235.7$ kHz, the demodulation frequency of the LvF signal is set as $f_2 = 1471.8$ kHz, and then the laser modulation frequency is set as $f_m = f_2 - f_1 = 1236.1$ kHz. The oscillation amplitude of the probe at f_2 can be obtained as[17]

$$A_2 = \frac{d\Delta F(z)}{dz} \frac{1}{2\sqrt{m^2(\widehat{\omega}_2^2 - \omega_2^2)^2 + \widehat{b}_2^2 \omega_2^2}} A_1, \tag{S15}$$

where m is the mass of the cantilever, ω_2 is the effective angular frequency of the second-order resonance mode, $\widehat{\omega}_2$ is the effective angular frequency at f_2 under external force, $\widehat{b}_2$ is the effective damping coefficient of the cantilever at f_2 under the external force, and A_1 is the carrier amplitude. Since f_2 is the demodulation frequency, the second-order resonance amplitude A_2 of the cantilever is retrieved to represent the LvF signal.

SI-7. Further explanation of the sideband demodulation

As shown in Fig. S4, the volume of sample material affected by the excitation light can be divided into three regions: the central region V_p right below the probe tip where the sample has the largest optothermal effect and the strongest LvF interaction with the probe, the intermediate region V_a where the material directly absorbs light but with negligible LvF interaction with the probe, and the thermal diffusion region V_d where the material receives heat not directly from the illumination but through heat diffusion from the nearby regions with higher temperature.

Fig. S4. Schematic of the tip-sample interaction in LvFM. V_p is the central region right beneath the tip with the strongest LvF response; V_a is the intermediate region where the sample directly absorbs light but with negligible LvF with the probe; V_d is the heat diffusion region where the sample material receives heat through diffusion from the central regions; f_1 is the tapping frequency of the probe, f_m is the modulation frequency of the excitation laser, d is the thickness of the sample, and Δh is the variation of the effective tip-sample distance under laser excitation.

When the sample is illuminated by a modulated laser beam, all the three regions have thermal responses with the same modulation frequency f_m. However, since the probe tip vibrates at tapping frequency f_1, only the response of the central region V_p contains a frequency component f_1. f_m and f_1 couple with each other, resulting in new vibration frequencies $f_2 = |f_m \pm f_1|$. Therefore, in LvFM, we can use a dual-modal cantilever with two mechanical eigenmode resonance frequencies f_1 and f_2, as schematically shown in Fig. 2(c). The modulation frequency f_m is chosen such that it satisfies $f_2 = |f_m \pm f_1|$. In this way, both the forces outside the central region V_p (which are not modulated by f_1) and the forces not influenced by the optothermal effect (which are not modulated by f_m) cannot respond and are excluded in the LvFM detection. Then, the LvF signal can be demodulated from

the resonance amplitude of the cantilever at f_2 with the best SNR.

SI-8. Spatial resolution of LvFM

The spatial resolution of LvFM can be analyzed as follows. Taking the radius of the probe tip apex as ~10 nm and the excitation laser spot as Gaussian profile (which are the cases in our setup), we can numerically calculate the contribution of each point ρ on the sample surface to the total tip-sample force, i.e., $F(\rho)/F$ or $F'(\rho)/F'$, by using the formulae and procedure described in the theoretical part of the paper and SI-5.
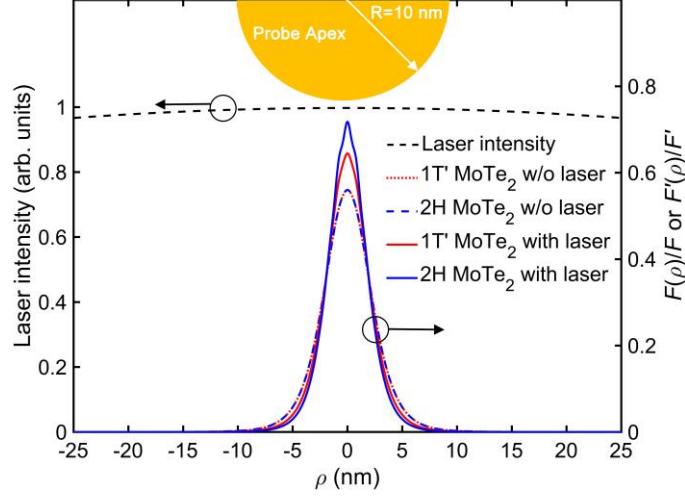
Fig. S5. Spatial distribution of tip-sample force beneath the probe tip. Black dashed line: intensity profile of the focused laser spot. Blue and red dashed lines: calculated distribution of tip-sample vdW force without laser illumination. Blue and red dashed lines: calculated distribution of the tip-sample LvF under laser excitation.

Specifically, let us consider a MoTe$_2$ film sample composed of 2H phase and 1T' phase, then a spatial distribution of the tip-sample force below the tip with and without light illumination can be obtained, as shown in Fig. S5. From the results, we can draw several important conclusions:

(1) All the tip-sample force distribution curves have sharp peaks in the very central area right beneath the tip. The full width at half maxima (FWHM) of each peak is only ~ 4 nm, which is even much smaller than the probe tip size (20 nm in diameter). This is unsurprising because the tip-sample vdW force is very sensitive to the tip-sample distance: as soon as the location moves far away from the tip, the interaction force drops down rapidly to vanish. Therefore, the FWHM of 4 nm can be a theoretical estimate of the spatial resolution of LvFM, which is close to the practical spatial resolution in our experiment of ~10 nm, as seen in Fig. 3(b). This also reveals an important fact that, unlike AFM or SNOM whose spatial resolutions are mainly determined by the probe tip size, the LvFM has an extremely high spatial resolution even smaller than the tip size, which is governed by the vdW force interaction law.

(2) Even though the spatial resolution of LvFM is very high, the two phases of MoTe$_2$ cannot be distinguished without light excitation, since their static vdW force responses are almost the same (as seen from the blue and red dashed lines in Fig. S5). Nevertheless, when an excitation light with Gaussian profile is applied, the magnitudes of LvF responses of the 2H and 1T' phases are both enhanced and exhibit remarkable difference in their peaks (as seen from the blue and red solid lines in Fig. S5), thanks to the distinct binding forces of molecules in the two phases. In this way, the two

phases can be discriminated.

The above analyses not only explain the theoretical origin of high spatial resolution of LvFM, but also reveals the contribution of light excitation for material discrimination.

SI-9. XRD characterization of the MoTe$_2$ sample

X-ray diffraction (XRD, smartlab, Rigaku) characterization of the MoTe$_2$ sample was performed, as shown in Fig. S6, which confirm the existence of 1T' phase and 2H phase regions in the sample. Moreover, the XRD spectra in Fig. S6 show that the two phases in sample are both polycrystalline monoclinic structures, with two distinct peaks near $2\theta = 12.712°$ and $25.487°$ corresponding to the (002) and (004) diffraction surfaces of the polycrystalline cubic structures of MoTe$_2$, respectively [JCPDS data card #15-0658]. The measured XRD data agree with literature reports[19], confirming the formation of 1T' and 2H phases in the MoTe$_2$ film. Based on the XRD data, we can calculate the grain sizes of the 1T' and 2H phases, which are listed in Table S1.
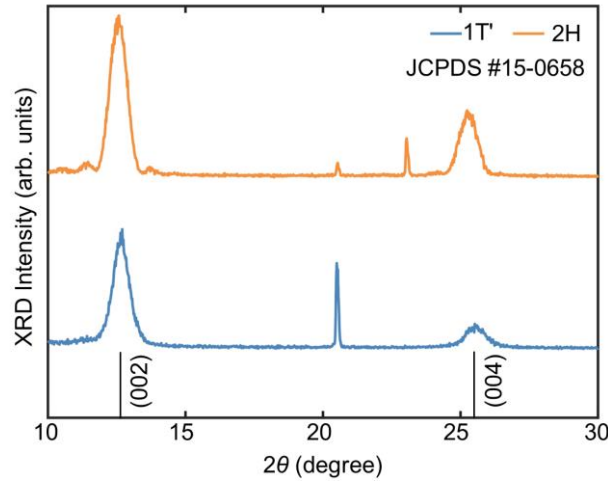
Fig. S6. XRD spectra of the 1T' and 2H phases of the MoTe$_2$ film grown on sapphire substrate.

Phase	2θ (°)	FWHM (°)	Grain size (nm)
1T'	12.70	0.696	11.357
2H	12.58	0.702	11.261

Table. S1. Measured crystallographic parameters of the 1T' and 2H phases of the grown MoTe$_2$.

SI-10. LvFM characterization of MoTe$_2$ under different excitation wavelengths

As discussed in the main text, the LvFM is a broadband technique insensitive to the wavelength of excitation light. The composition materials of a heterostructure can be discriminated provided that the optothermal effects of the composing materials can provide sufficiently large LvF contrast. To demonstrate this fact, we have measured LvF images of the MoTe$_2$ sample in the spectral range of 500 nm ~ 900 nm. The LvF mapping images of 9 excitation wavelengths are given in Fig. S7, where the LvF contrast of U_H/U_T is calculated and noted in each sub-figure. These data are also the source data for drawing the LvF contrast curve in Fig. 4f in the main text.
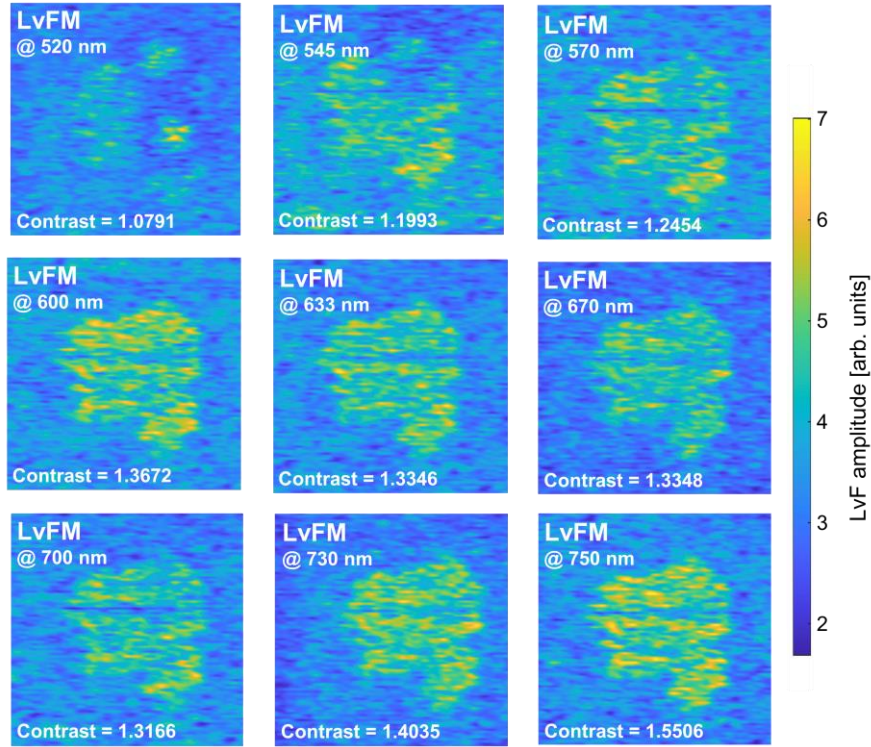
Fig. S7. LvF mapping images of the MoTe$_2$ film under 9 different excitation wavelengths.

SI-11. More characterization results of the WS$_2$/h-BN heterogenous materials

We use LvFM to characterize a heterostructure of multilayer h-BN and WS$_2$ nanosheets. As shown in Fig. 4h, the light absorption coefficients of WS$_2$ and h-BN are quite different in the spectral range of 600 ~ 680 nm, which form the basis for large LvF response contrast. In addition to the LvF mapping results under the excitation wavelength of 633 nm in Fig. 4i, we have also measured the LvF mapping results at 600 nm and 680 nm, as shown in Fig. S8. In all these images, the h-BN and WS$_2$ regions can be clearly distinguished with a high spatial resolution of ~10 nm.
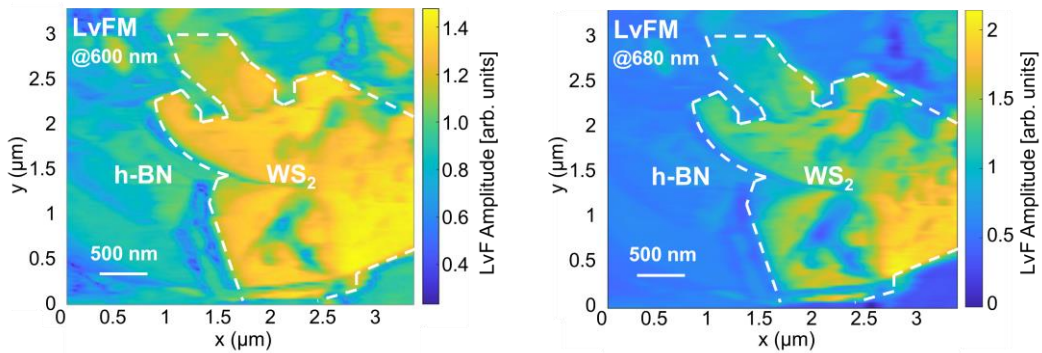
Fig. S8. LvF mapping images of the WS$_2$/h-BN heterostructure under the excitation wavelengths of 600 nm (left) and 680 nm (right).

Moreover, we have measured the Raman spectra and confocal Raman mapping results of the h-BN/WS$_2$ heterogenous material, as shown in Fig. S9, which confirm the compositions of h-BN and WS$_2$ in the sample.
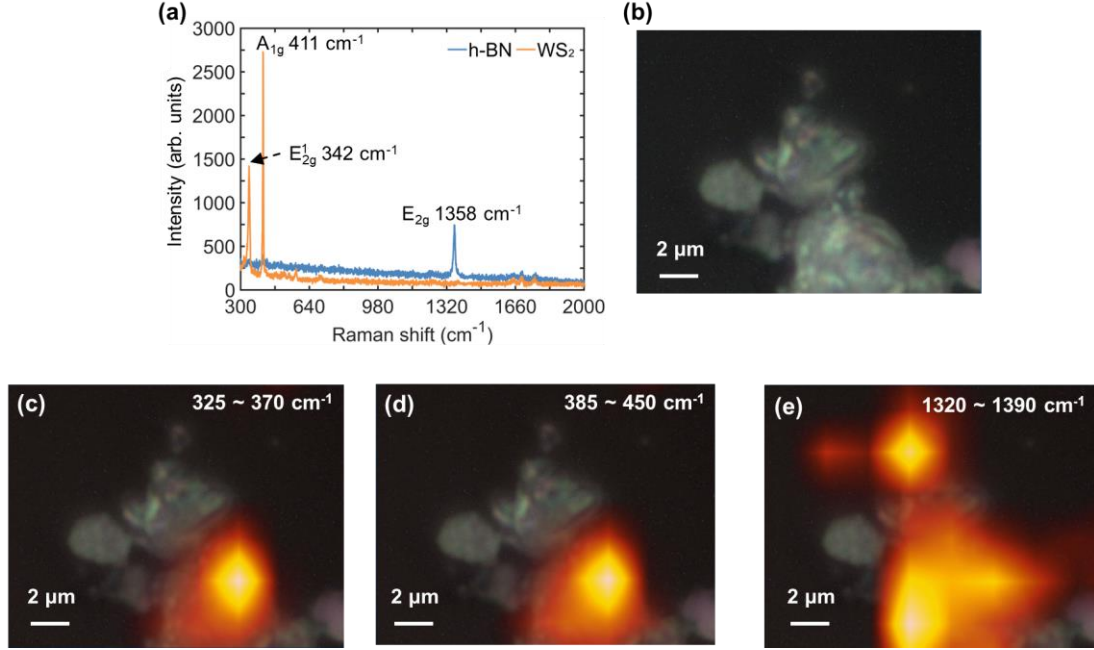
Fig. S9. (a) Raman spectra of the h-BN/WS$_2$ heteromaterial sample investigated in Fig. 4. (b) Optical microscopic image of the sample. (c), (d) and (e) are the overlaid images of the optical image of the sample and its confocal Raman mapping results obtained in the 325~370 cm^{-1}, 385~450 cm^{-1}, and 1320~1390 cm^{-1} integration intervals, respectively.

SI-12. LvFM characterization of Au nanoparticles and PS nanospheres

We deal with a mixture of Au NPs and polystyrene (PS) NPs with the similar diameters ~100 nm, which are randomly dispersed onto the surface of a glass substrate. Both AFM and LvFM were employed to characterize the NP ensembles. The LvFM experimental parameters are: a 532 nm excitation laser of 1.0 mW, an Au probe from NANOSENSORS™ with f_1=231 kHz, Q_1= 438, k_1 = 40 N/m, f_2=1475 kHz, Q_2=642, and tip curvature radius ~ 25 nm, the setpoint of 60%, and the modulation frequency $f_m = f_2 - f_1$ = 1244 kHz.

The AFM topography image, AFM phase image, and LvFM image are shown in Figs. S10(a), S10(b), and S10(c), respectively. Clearly, the two types of NPs cannot be distinguished by AFM topography. Surprisingly, they cannot be distinguished by AFM phase imaging either, whose phase difference is only ~4%, meaning that the viscous/ adhesion forces between the tip and the two kinds of NPs are quite similar. In contrast, with LvFM imaging, the two types of NPs can be clearly distinguished, whose LvF response difference is ~42%. To cross-check that the NPs at positions (i) and (ii) are indeed different kinds of NPs, we have used micro-photoluminescence (PL) spectroscopy to get their PL spectra, as shown in Fig. S10(d), from which Au NP and PS NP can be identified.

Moreover, to check the repeatability of the measurement, we have characterized multiple NPs in the sample with LvFM and make statistics of the LvF versus particle sizes and types, as shown in Fig. S10(e). Clearly, the data points are divided into two distinct groups, one for Au NPs with lower LvF response and the other for PS NPs with stronger LvF response. The LvF dependence on the particle size is not evident. This experiment is a good example of using LvFM to distinguish metal and polymer.
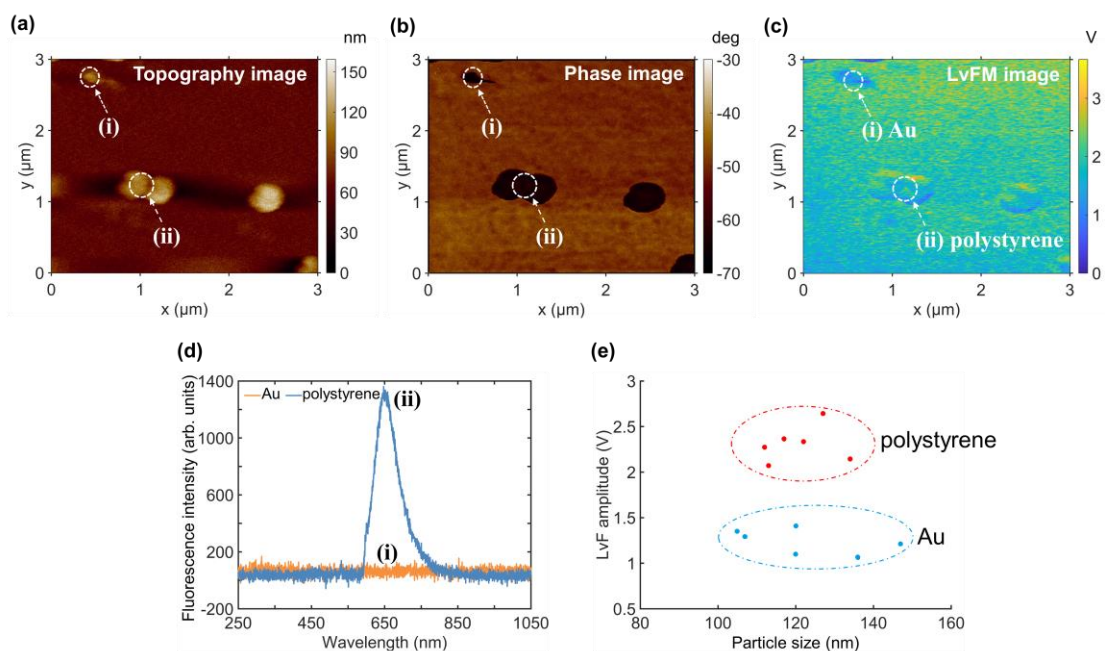
Fig. S10. (a) AFM topography image, (b) AFM phase image, and (c) LvFM image of the Au and polystyrene (PS) NPs randomly dispersed on the surface of a glass substrate. (d) PL spectra of NPs taken from positions (i) and (ii). (e) Comparison of the measured LvF signals of the two types of NPs.

SI-13. LvFM characterization of organic compounds

We characterize photoresists, a class of light-sensitive organic compounds. For this purpose, a heterogeneous structure containing two types of photoresists, AZ4620 (a positive photoresist) and SU8 (a negative photoresist) was prepared, as shown in Fig. S11(a). In this structure, SU8 is filled in a small volume of $12 \times 12 \times 7$ μm^3 in the AZ4620 layer, as seen in the optical microscopic image in Fig. S11(b). AFM topography imaging and LvFM image results of the sample are shown in Figs. S11(c) and S11(d), respectively. Clearly, while the topography is rather flat, one can still distinguish the two photoresist areas according to their evident LvF response contrast. It is worth noting that in this experiment, a 532 nm laser of 1.1 mW was employed. Although the vibrational absorption energy levels of the organics are mainly in infrared band, the LvF response under visible light excitation is strong enough for material discrimination.
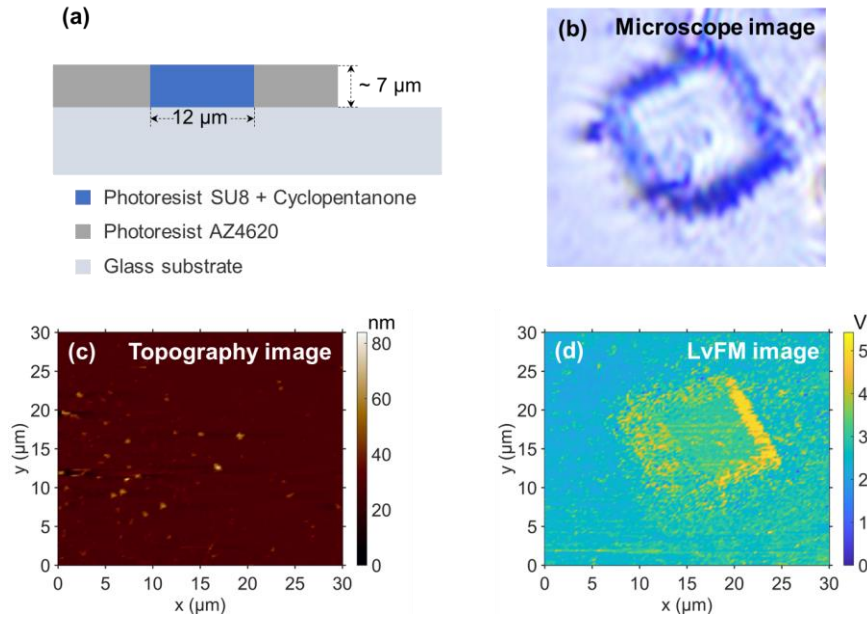
Fig. S11. (a) Schematic of the heterogeneous structure containing AZ4620 and SU8 photoresists. (b) Optical microscopic image, (c) AFM topography image, and (d) LvFM image of the sample.

SI-14. LvFM characterization of metal oxides

Ho_2O_3 and Al_2O_3 films were prepared and characterized by LvFM using a 633 nm excitation laser. The scanning areas are across the edges of the films. The AFM topography, AFM phase, and LvFM image of the Ho_2O_3 film are shown in Figs. S12(a) ~ S12(c), respectively. According to the AFM topography, the Ho_2O_3 film is ~140 nm thick and there is a stacking area of ~2 μm wide in the Ho_2O_3 film. In the AFM phase image, the contrast of different areas is rather low. But in LvFM image, the LvF difference/contrast between Ho_2O_3 and the substrate is very clear. Moreover, the LvF strength is dependent on the thickness of the film: in thicker film area, the LvF amplitude is smaller, due to the strong absorption of Ho_2O_3 to visible light when it passes through the film from the bottom side (note that ~640 nm is one of the absorption bands of holmium ions). This shows that LvFM can not only discriminate different materials, but also has the potential to resolve the thickness difference of the sample material.

The same characterization procedure has been conducted on a Al_2O_3 film, as shown in Figs. S12(d) ~ S12(f). The major difference from the Ho_2O_3 results is that the LvFM image contrast is lower, because the LvF response difference between Al_2O_3 film and the quartz substrate are not so large as that between Ho_2O_3 and quartz.
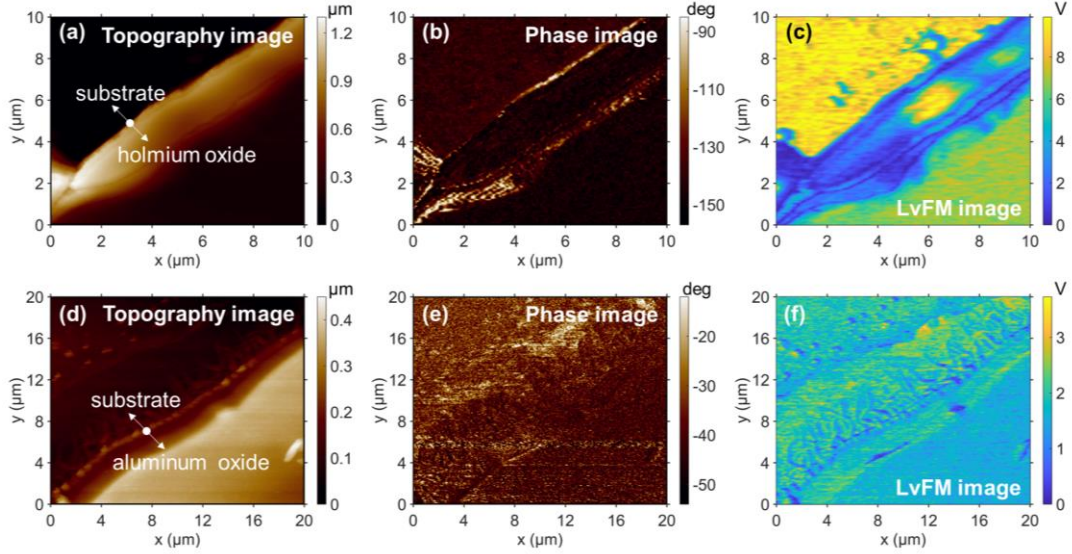
Fig. S12. (a) AFM topography, (b) AFM phase, and (c) LvFM images of a Ho_2O_3 film. (d) AFM topography, (e) AFM phase, and (f) LvFM images of a Al_2O_3 film.

SI-15. LvFM characterization of single walled carbon nanotubes (SWCNTs)

The electronic properties of SWCNTs strongly depend on their chiral structures, which could be semiconducting or metallic with quite different electronic state densities and optical properties. Therefore, we have tried to use LvFM to identify these two types of SWCNTs. By carrying out a large number of experiments, we have found that the LvF responses of monodispersed SWCNTs with similar diameters may differ from each other significantly. Figure S13 shows an example of the LvFM image of two SWCNTs under the same light excitation. Clearly, the LvF responses of SWCNTs (i) and (ii) are quite different, whose difference is larger than both AFM topography and AFM phase. But due to limited time, we have not finished the thorough investigation on SWCNTs yet. We have not characterized the chirality of these SWCNTs by other means such as TEM, STM, and Raman. The connection of LvF response of specific SWCNT to its chirality property has not been established. But the obtained results already show that LvFM has the potential to distinguish different SWCNTs, which will be an important research task of us in the future.
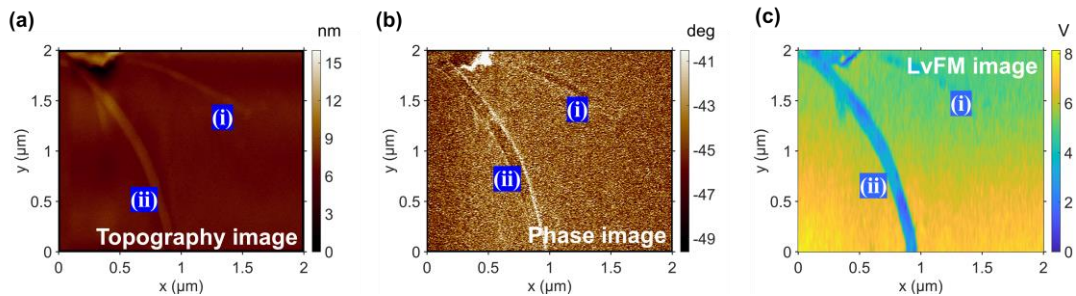

Fig. S13. (a) AFM topography, (b) AFM phase image, and (c) LvFM image of two SWCNTs.

SI-16. LvFM characterization of nanodefects in van der Waals materials

The mixture of two types of multilayered van der Waals materials prepared by mechanical exfoliation, GaS and NbS_2, is characterized by LvFM. The AFM topography and LvF image of the sample are shown in Fig. S14. It is seen that nanodefects can be probed by LvFM, some of which

can also be observed in AFM topography while some others cannot if they exist in flat area. Even for humps, some have no LvF contrast with the surrounding material (meaning their compositions the same), while some others have large LvF contrast (indicating the heterogenous materials). The detailed study of the types and forms of nanodefects with LvFM needs an in-depth investigation, which will be our work in the future. Nevertheless, these preliminary results already show that LvFM is a promising tool for finding and identifying nanodefects such as bubbles, wrinkles, or other impurities in van der Waals materials.
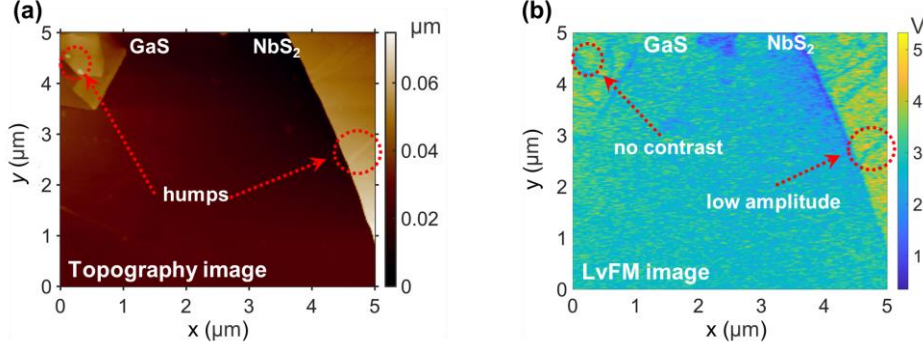

Fig. S14. (a) Topography and (b) LvF image of GaS and NbS$_2$ materials.

SI-17. Dependence of the LvF signal on the tip-sample distance

To show the dependence of the LvF detection on the tip-sample distance, we have performed more experiments on the LvF response of the MoTe$_2$ film with the same experimental conditions as those adopted in Fig. 3. Firstly, we tested the LvF response difference when the probe approaches the sample surface to work in the LvFM mode (tapping mode with setpoint ~60%) and is lifted off from the sample, as shown in Fig. S15(a). Clearly, by repeatedly switching the probe between the two states many times, we can see that the LvF signal appears only when the probe works in the LvFM mode in the vdW force interaction zone.

In Fig. S15(b), we also tested the variation of the LvF response during the process when the probe (in tapping mode) is launched onto or lifted off from the sample surface. Note that the horizontal axis z of Fig. S15(b) is the displacement of the dither piezo driving the probe. Therefore, it indicates the relative displacement of the probe, but not the absolute tip-sample distance. Actually, the absolute tip-sample distance cannot be measured or calibrated anyway. The only way to monitor the tip-sample distance is to control the setpoint, as discussed before. During the measurement of Fig. S15(b), with the decrease of z, the setpoint also decreases. When the setpoint approaches 60% as we adopt in LvFM, the displacement of the dither piezo is now denoted as $z = 0$. When $z < 0$, the probe is closer to the surface, and vice versa. It is seen that LvF signal only appears in the close vicinity of the sample surface and reaches maximum when $z \sim 0$ nm (corresponding to setpoint ~60%), which validates the LvFM mechanism that the probe must work in the vdW force interaction zone. The sensitivity to the tip-sample distance can be evaluated from the slope of the curve.
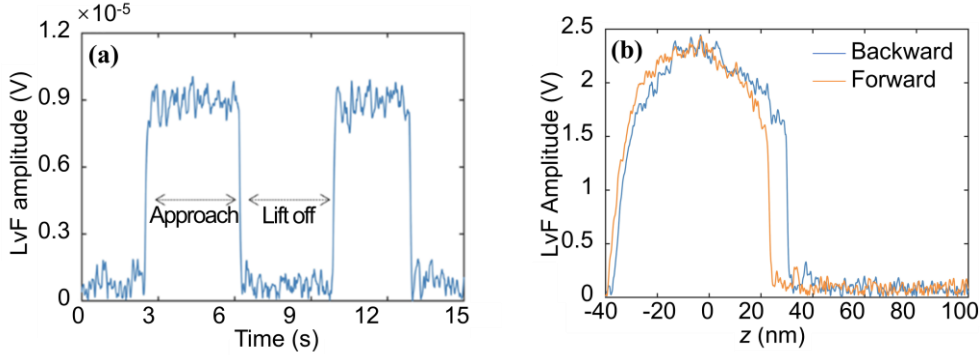
Fig. S15. Measured LvF signals from the MoTe$_2$ film with the same experimental conditions as those adopted in Fig. 3. (a) Detected LvF signals when the probe approaches or is lifted off from a sample surface. (b) Variation of the LvF signal when the probe is launched onto or lifted off from a sample surface.

Moreover, we have tried different setpoints in the modulation/demodulation, as shown in Fig. S16. At each setpoint, we scanned the laser modulation frequency f_m to get the dependence of LvF amplitude on f_m. It is seen that with the increase of the setpoint, the peak f_m moves to lower frequency. According to AFM theory, this shift represents the increase of the ratio of attractive force to repulsive force. Since the attractive force in this tip-sample interaction region is mainly the vdW force, it verifies again, from another point of view, that LvF is in nature the vdW force.
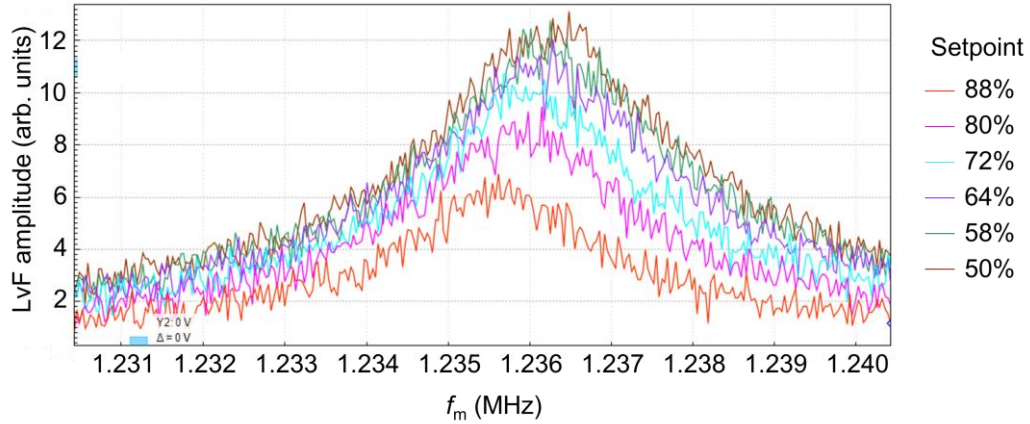

Fig. S16. Measured dependence of the LvF amplitude on the laser modulation frequency f_m at different setpoints.

According to the above tests, we can see that the tip-sample distance and the working mode of probe are essential to realize successful detection of the LvF signal.

References

1   Wang, H., Wang, L. & Xu, X. G. Scattering-type scanning near-field optical microscopy with low-repetition-rate pulsed light source through phase-domain sampling. *Nature Communications* **7**, 13212 (2016).

2   Zhang, S. *et al.* Nano-spectroscopy of excitons in atomically thin transition metal dichalcogenides. *Nature Communications* **13**, 542 (2022).

3   Najmaei, S. *et al.* Vapour phase growth and grain boundary structure of molybdenum disulphide atomic layers. *Nature Materials* **12**, 754-759 (2013).

4 Huang, Y. L. *et al.* Bandgap tunability at single-layer molybdenum disulphide grain boundaries. *Nature Communications* **6**, 6298 (2015).

5 Morita, S., Giessibl, F. J., Meyer, E. & Wiesendanger, R. *Noncontact Atomic Force Microscopy: Volume 3.* (Springer, 2015).

6 Dazzi, A. & Prater, C. B. AFM-IR: Technology and Applications in Nanoscale Infrared Spectroscopy and Chemical Imaging. *Chemical Reviews* **117**, 5146-5173 (2017).

7 Mathurin, J. *et al.* Photothermal AFM-IR spectroscopy and imaging: Status, challenges, and trends. *Journal of Applied Physics* **131**, 010901 (2022).

8 Yang, J., Hatcherian, J., Hackley, P. C. & Pomerantz, A. E. Nanoscale geochemical and geomechanical characterization of organic matter in shale. *Nature Communications* **8**, 2179 (2017).

9 Lee, H. *et al.* Tip-enhanced photoluminescence nano-spectroscopy and nano-imaging. *Nanophotonics* **9**, 3089-3110 (2020).

10 Zhang, Z., Sheng, S., Wang, R. & Sun, M. Tip-Enhanced Raman Spectroscopy. *Analytical Chemistry* **88**, 9328-9346 (2016).

11 Otter, L. M. *et al.* Nanoscale Chemical Imaging by Photo‐Induced Force Microscopy: Technical Aspects and Application to the Geosciences. *Geostandards and Geoanalytical Research* **45**, 5-27 (2021).

12 Rajapaksa, I., Uenal, K. & Wickramasinghe, H. K. Image force microscopy of molecular resonance: A microscope principle. *Appl Phys Lett* **97** (2010).

13 Johansson, P. & Apell, P. Geometry effects on the van der Waals force in atomic force microscopy. *Physical Review B* **56**, 4159 (1997).

14 Garcıa, R. & Perez, R. Dynamic atomic force microscopy methods. *Surface science reports* **47**, 197-301 (2002).

15 Dazzi, A., Glotin, F. & Carminati, R. Theory of infrared nanospectroscopy by photothermal induced resonance. *Journal of Applied Physics* **107**, 124519 (2010).

16 Jahng, J., Potma, E. O. & Lee, E. S. Tip-Enhanced Thermal Expansion Force for Nanoscale Chemical Imaging and Spectroscopy in Photoinduced Force Microscopy. *Anal Chem* **90**, 11054-11061 (2018).

17 Jahng, J., Kim, B., Lee, E. S. & Potma, E. O. Quantitative analysis of sideband coupling in photoinduced force microscopy. *Physical Review B* **94**, 195407 (2016).

18 Garcia, R. & Herruzo, E. T. The emergence of multifrequency force microscopy. *Nat Nanotechnol* **7**, 217-226 (2012).

19 Ueno, K. & Fukushima, K. Changes in structure and chemical composition of α-MoTe$_2$ and β-MoTe$_2$ during heating in vacuum conditions. *Applied Physics Express* **8**, 095201 (2015).